Eco-Degradable and Flexible Solid-State Ionic Conductors by Clay-Nanoconfined DMSO Composites

Seunghyeon Lee, Hong Seop Hwang, Whirang Cho, Daseul Jang, Taesik Eom, David C. Martin, Jeong Jae Wie, and Bong Sup Shim*

Solid-state electrolytes can alleviate the safety issues of electrochemical energy systems related to chemical and thermal instabilities of liquid electrolytes. While a liquid provides seamless ionic transport with almost perfect wettability between electrodes, a solid-state electrolyte needs to demonstrate at least comparable electrochemical performance to liquid electrolytes as well as mechanical robustness and flexibility. Here, the facile preparation of montmorillonite (MMT)/dimethyl sulfoxide (DMSO) nanocomposites is reported, which show high ionic conductivities, mechanical strengths, and thermal stabilities by forming nacre-mimetic "brick-and-mortar" structures. The molecularly confined structures of DMSO are confirmed by X-ray diffraction peaks with d-spacings of interplanar spacing that are slightly larger than MMTs. The MMT/DMSO composites have mechanical strengths and toughnesses of 55.3 \pm 4.8 MPa and 210.2 \pm 32.6 kJ m⁻², respectively. The ionic conductivity is $\approx 2 \times 10^{-4}$ S cm⁻¹ at room temperature, and their thermal stability is in the range of -100 to 120 °C. The optical translucency, on-demand eco-degradability, and solution processability together make the MMT/DMSO composites unique materials with a wide range of solid-state electrochemical applications including batteries.

1. Introduction

Conventional battery industries have primarily relied on liquid electrolyte systems because of the excellent wettability and superior ionic conductivity of liquids. However, the chemical and

S. Lee, H. S. Hwang, Dr. W. Cho, D. Jang, T. Eom, Prof. B. S. Shim Department of Chemical Engineering

Inha University

100 Inha-ro, Michuhol-gu, Incheon 22212, South Korea

E-mail: bshim@inha.ac.kr

Dr. W. Cho

Department of Chemistry

American University

4400 Massachusetts Avenue NW, Washington, DC 20016, USA

D. Jang, Prof. D. C. Martin

Department of Materials Science and Engineering

University of Delaware

201 DuPont Hall, Newark, DE 19716, USA

Prof. J. J. Wie

Department of Polymer Science and Engineering

Inha University

100 Inha-ro, Michuhol-gu, Incheon 22212, South Korea

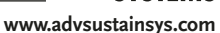
The ORCID identification number(s) for the author(s) of this article can be found under https://doi.org/10.1002/adsu.201900134.

DOI: 10.1002/adsu.201900134

thermal instabilities of liquid electrolytes can cause significant drawbacks, particularly for safety. Solid-state electrolyte can overcome these limitations. Typically, solid-state electrolytes have five classifications based on the material constituents:^[1] inorganic electrolytes, polymer electrolytes, hybrid electrolytes, gel–polymer electrolytes, and hybrid quasisolid electrolytes. Hybrid electrolytes are composed of both organic and inorganic materials, and gel–polymer electrolytes and hybrid quasisolid electrolytes are mixtures of organic and inorganic materials with liquid electrolytes, respectively.

Next-generation sodium-ion batteries (SIB) have similar working mechanisms and cycling stability as conventional lithium-ion batteries (LIB). They also have several significant advantages including the natural abundance and widespread geological distribution of the sodium resource, low cost, and low toxicity.^[2–10] Many studies have attempted to develop suitable materials for SIBs and

have recently focused on improving their reliability and practicability.[11-18] Currently, the state-of-the-art inorganic solid sodium electrolyte is the Na superionic conductor (NASICON) with the $Na_{1+3x}Zr_2(P_{1-x}Si_xO_4)_3$ structure. The ionic conductivity of NASICON reaches 10^{-3} S cm⁻¹ at $T \ge 65$ °C.^[19] However, NASICON is a rigid and brittle inorganic material and is intrinsically limited for the applications in flexible batteries. Also, the intrinsically large interfacial impedance between the inorganic solid electrolyte and solid electrodes deteriorates its electrochemical properties. [5,20,21] Furthermore, the prevention of dendrite evolution is still one of the most challenging issues. [22,23] Meanwhile, low mechanical integrity, [24] ionic conductivity, and oxidation resistivity eclipse the other advantages of organic polymer electrolytes which include flexibility, lightweight, good adhesion, and wettability to electrodes. Hybrid, gel-polymer, and hybrid quasisolid electrolytes take advantage of both components. For hybrid electrolytes, the addition of inorganic materials into polymer increases Young's modulus, but it cannot exceed that of pure inorganic components.^[24-26] For gel-polymer electrolytes, the polymeric network provides mechanical stability for the mobile liquid electrolyte.^[27] For hybrid quasisolid electrolytes, the addition of liquid electrolyte improves the ionic conductivity by improving wetting or interfacial contact of the inorganic component to the electrodes.



ADVANCED SUST AINABLE SYSTEMS

However, as the path for ion migration becomes more complicated than for pure liquid electrolytes, ion transport is slow.^[28]

The important governing parameters to develop high-performance solid-state electrolytes include excellent mechanical integrity and thermal stability, high ionic conductivity and selectivity, low cost, intimate integration with electrodes, and environmental friendliness.[29-34] For solid-state electrolyte membranes, the mechanical properties should be robust enough to avoid the risk of dendrite growth. For example, dendrite growth can be suppressed with stiffer electrolytes than the metal electrode itself, 6 GPa for LIB.[35] In the case of solid electrolytes with excellent ionic conductivities, other challenges arise such as high interfacial impedances between electrodes and electrolyte (as in NASICON) or high operating temperatures due to the limitation of the ionic mobility (as with poly(ethylene oxide) (PEO)). Therefore, intimate interfacial contact between electrolyte and electrode as well as room temperature operability are crucial for designing desirable solid-state electrolytes. In addition, environmentally friendly materials are another merit in terms of replacing toxic organic solvents, which may require costly processes.

Natural nacre, in which 2D calcium carbonate aragonite platelets are mixed with organic molecules by forming "brickand-mortar" structures, exhibits a toughness that is three orders of magnitude higher than its constituents. Although the fraction of organic molecules is only 5% in nacre, they play an important role in hybridizing properties by allowing the strain fracture energy dissipation through frictional sliding of the platelets against each other. [36-39] Inspired by the structures of natural nacre, various preparation strategies have been explored to develop nanocomposites with unique properties including layer-by-layer (LBL) deposition, [40-42] freeze-drying, [36,43] hot-press-assisted slip casting, [44] freezethawing, [45,46] dry casting, [47-49] and warm-pressing. [50] The functional nanobuilding blocks of these nacre-inspired composites could be extended to various inorganic 2D nanoplatelets including clay,[39,40,42] boron nitride,[51,52] layered double hydroxides (LDH),[53-55] graphene,[47,48,56,57] and Al₂O₃. [36,43,49,58] These inorganic components are combined with polymeric mortars such as chitosan, [48,49] polyvinyl alcohol (PVA), [42,47,53,55] poly(methylmethacrylate) (PMMA), [36,58,59] and poly (diallyldimethyl ammonium chloride) (PDDA). [60,61]

Among the 2D nanoplatelets, montmorillonite (MMT) clay is a nanothin crystalline material roughly 1 nm in thickness. MMT is suitable for preparing multifunctional nanocomposites with inherently useful features, such as high surface area, [62] gas barrier property, [63] flame retardant features, [64] and thermal stability.^[65] It is also abundant and inexpensive.^[66] The natural Na+-MMT nanoclay, which has its chemical structure of $((Na,Ca)_{0.33}-(Al_{2-w}Mg_v)Si_4O_{10}(OH)_2\cdot nH_2O),^{[67-69]}$ is hydrophilic and miscible with polar polymers such as PEO and PVA.[70] For compatibility with most hydrophobic polymers, organically modified clays have been employed.^[71,72] However, the material properties of the isotropic clay composites prepared by the conventional processes were limited because of the difficulty in raising the MMT loading.^[73] On the contrary, nacre-inspired nanocomposites with clay contents up to 80% have shown enhanced thermal and mechanical properties.^[72,74] While well-exfoliated clay is a necessary component for preparing brick-and-mortar structures, small amounts of organic binders are also crucial for defining the performances of the resulting composites. For micrometer-sized platelets such as alumina or boron nitride, high molecular weight polymers are preferred to comprise the nacre structure.^[36,49,51,52] However, for nanosized MMTs, the long polymer chains inhibit uniform intercalation into nanogallery spaces of MMTs even with in situ polymerization.^[74,75] Moreover, the dispersion between polymer matrix and MMT tends to induce phase separation, which decreases transparency.^[76]

In this study, we introduce a quasi-solid-state ionic conductor composed of MMT and dimethyl sulfoxide (DMSO), a common polar aprotic solvent, as organic binders because of its relatively compact structure and low toxicity as well as its capacity of forming hydrogen bonds.^[77] A novel MMT-DMSO nanocomposite film, in which DMSO molecules are structured by oriented confinement, was prepared by a facile vacuum-assisted assembly method.^[78] The orderly layered structures of the MMT/DMSO composites were demonstrated by using X-ray diffraction spectroscopy (XRD) and scanning electron microscopy (SEM). Also, the thermal properties of the MMT/DMSO composites were further investigated by using thermogravimetric analysis (TGA) and differential scanning calorimetry (DSC), which confirmed that the optimally designed MMT/DMSO composites could be used up to 120 °C without significant thermal degradation. The MMT/DMSO composites show pronounced solid-state ionic conductivities up to $\approx 2.06 \times 10^{-4} \text{ S cm}^{-1}$ in the through-plane direction at room temperature. Moreover, the MMT/DMSO composites have mechanical robustness as well as flexibility, which correlates with their molecularly ordered structure. With the high content of clay and with the stratified nanostructures of MMTs, diffusion of both oxygen and flammable volatiles were also restricted and thus provided flame retardant properties even with DMSO. These multifunctional MMT/DMSO composites are eco-materials because on-demand degradability can be achieved readily by feeding them to superworms. Overall, the nacre-mimetic MMT/DMSO composites with unique combinations of thermal, mechanical, and electrochemical performances offer new possibilities for the development of eco-friendly solid-state electrolytes.

2. Experimental Section

2.1. Materials

The sodium montmorillonite nanoclay (Na⁺-MMT) (Na-Cloisite, Nanokor Co.) and dimethyl sulfoxide (DMSO, \geq 99.5%, Daejeong) were used as received. The chemical structure of the montmorillonite clay is (Na,Ca)_{0.33}(Al,Mg)₂Si₄O₁₀(OH)₂·nH₂O. The Na⁺-MMTs were used for our study. An MMT/DMSO suspension was vacuum-filtrated by using polytetrafluoroethylene (PTFE) membrane (pore size: 0.45 μ m, Millipore). Stainless-steel thumbtacks purchased from a local stationery store were used as both working and counter electrodes.

2.2. Exfoliation of MMT Nanoclay Solution

For liquid-phase exfoliation, MMT nanoclay powder was dissolved in DI water (0.5 wt%) under agitation for 30 min by

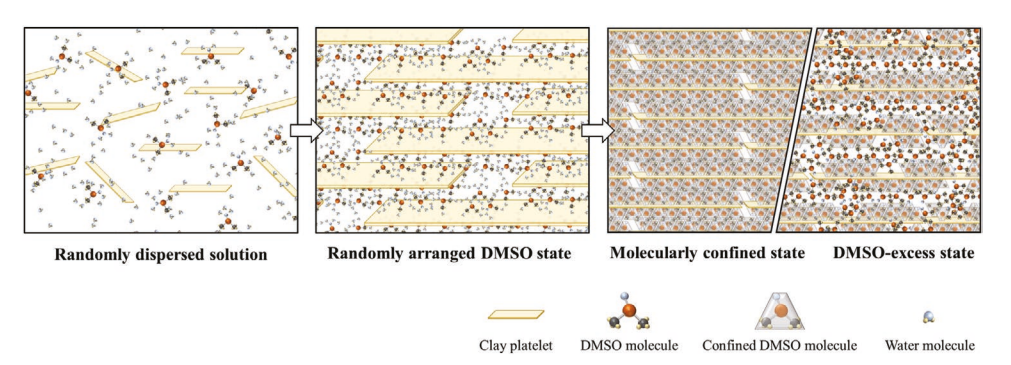


Figure 1. Scheme of the fabrication process and the molecular structure of each state.

high shear blending (2400 W). The dispersed solution was centrifuged at $2700 \times g$ for 15 min to precipitate the unexfoliated MMT particles, followed by the collection of the supernatant by pipette. The supernatant was stable for more than a month without noticeable precipitation at room temperature.

2.3. Fabrication of MMT/DMSO Composites

The synthesis of MMT film and MMT/DMSO composites started with the gradual addition of a required amount of DMSO in a range from 0 to 50% into the 20 mL of MMT dispersed solution followed by stirring for 30 min to obtain MMT/ DMSO hybrid suspension. The obtained suspension was subsequently self-assembled into the MMT/DMSO composites via vacuum-assisted filtration process. The cakes and membrane together were then further dried at 60 °C in a convection oven for 6 h to remove water. After drying, the MMT film and all MMT/DMSO composites could be readily detached from the membrane as freestanding films. The MMT/DMSO composites were names as MMT/DMSO-5, MMT/DMSO-10, MMT/DMSO-20, MMT/DMSO-35, and MMT/DMSO-50 depending on the relative input amount of DMSO as a volume percentage to the total MMT/DMSO mixture solution before the filtration process. The thicknesses of the final MMT film and MMT/DMSO composites varied from 40 to 320 µm depending on the amount of DMSO (Figure 1; Figure S1, Supporting Information).

2.4. On-Demand Eco-Degradability Test

Each set of MMT/DMSO composites films were used to test on-demand degradability by the superworm feeding method. At room temperature, 40 superworm larvae were put in a cage with a mesh floor to remove feces. MMT films and MMT/ DMSO composites were weighed and placed into the cage containing 40 superworms for 4 h at room temperature. The cut pieces of residual films were collected after being eaten by the worms, and the net weight changes were determined.

2.5. Characterization

The layered structure of nanocomposite was evaluated by XRD (X'Pert PRO MRD (Philips)). The XRD profile was

recorded in a reflection mode in the range of 3°-40° at a scan speed of 0.07° s⁻¹. The X-ray was generated by Cu K α radiation (1.548 Å) under a voltage of 40 kV and a current of 30 mA. The d-spacing of MMT was calculated from the peak position of the XRD patterns using Bragg's equation $d = 2\pi/q$, where the wavenumber q is defined as $q = (4\pi/\lambda)$ sin $(\theta/2)$, where λ is the X-ray wavelength and θ is the scattering angle. The layered morphology of the films was examined by performing SEM measurements on a Hitachi SU8010 with an accelerating voltage of 5 kV. The specimens were coated with Pt to avoid charging. DSC measurements on the DMSO intercalated MMT samples were performed with a DSC200F3 (Netzsch) under a nitrogen atmosphere. The DSC thermograms were recorded at a scanning rate of 10 °C min⁻¹ from −100 to 120 °C. TGA and differential thermal analysis (DTA) were tested on a TG 209 F3 (Netzsch) to measure the amount of DMSO intercalated into the MMT platelets. The samples were heated from room temperature up to 500 °C at a rate of 10 °C min⁻¹ in N₂ flow. Electrochemical impedance spectroscopy (EIS) of the films was performed at 100 mV rms of AC voltage from 1 to 100 kHz of the frequency with a two-electrode system on a Gamry reference 600 potentiostat (Gamry) at room temperature. Stainless-steel electrodes were used for electrochemical characterization. The flameretardant properties were tested with a torch using butane gas as fuel.

We have fitted the impedance spectra to equivalent circuit models expressed with the combination of resistances and capacitors (Figure S7, Supporting Information). The "goodness-of-fit" parameter obtained from the fitting is Chi-squared that shows the difference between observed values and those expected theoretically. Thus, "goodness of fit" should be zero for ideal matching between the calculations and the experiments. Here, as the goodness of fit is Chi-squared, it is the calculated sum of the weighted residuals defined as following

$$\chi^{2} = \sum_{i=1}^{N} w_{i}^{2} \left[\left(Z_{\text{meas}_{\text{real}}} - Z_{\text{fit}_{\text{real}}} \right)^{2} + \left(Z_{\text{meas}_{\text{imag}}} - Z_{\text{fit}_{\text{imag}}} \right)^{2} \right]$$
(1)

where the weighting (w_i) is calculated with Z_{mod} weighting as follows

$$w_i = \frac{1}{\sqrt{Z_{\text{meas}_{i,\text{real}}}^2 + Z_{\text{meas}_{i,\text{imag}}}^2}} \tag{2}$$

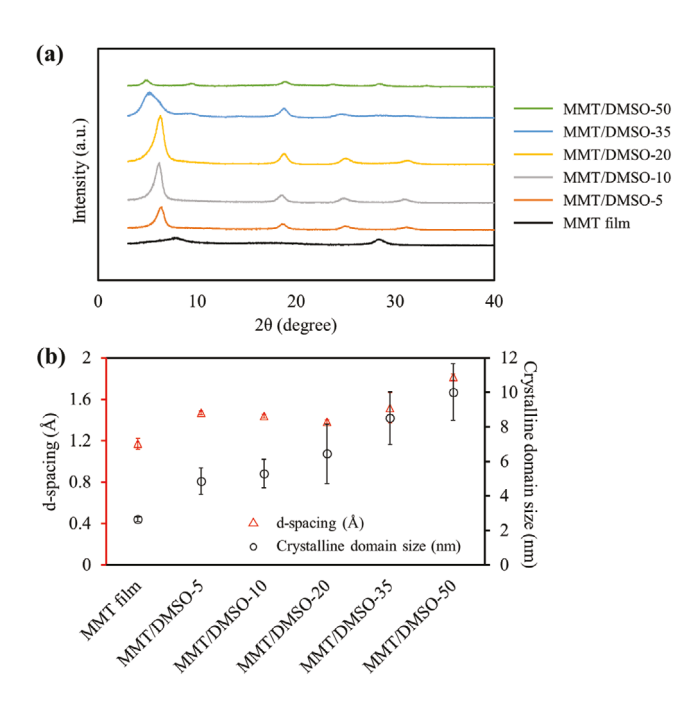


Figure 2. a) XRD patterns of MMT film and MMT/DMSO composites. b) Interplanar spacings and domain size of the MMT/DMSO composites with varying DMSO content.

3. Results and Discussion

3.1. Nanostructures of MMT/DMSO Composites

MMT nanoplatelets were organized into macroscopic layered structures with degrees of DMSO content. The nanostructural features as well as physicochemical interaction between MMTs and DMSO determine the multifunctional performances. Figure 2 shows the XRD patterns, corresponding interplanar distance between MMT galleries, and the crystalline domain size of MMT/DMSO composites. These were calculated from a peak position and a full width at half-maximum (FWHM) of the first reflection peak in the diffraction angle range between 5° and 9°. As shown in Figure 2a, the pristine MMT film shows a rather broad reflection peak indicating irregularly stacked structures compared to the

sharp and well-defined peaks of MMT/DMSO composites upon the addition of DMSO up to 35%. The interplanar distance, or *d*-spacing, can be obtained from Bragg's Law. The corresponding *d*-spacing of pristine MMT film is expanded from 1.17 up to 1.82 Å by the addition of DMSO. However, the *d*-spacing slightly decreased when the DMSO content increased from 5% to 20%, followed by a further increase with excess DMSO. These results suggest that the system is further confined with a certain amount of organized DMSO molecules that exist between the MMT layers. The average size of crystal or domain (τ) can be calculated by the Scherrer equation

$$\tau = \frac{K\lambda}{\beta \cos \theta} \tag{3}$$

where K is a dimensionless shape factor, λ is the wavelength of X-radiation, and β is FWHM. We set the K as 0.94, which corresponds to a combination of the tetrahedral and octahedral structure of MMT crystal. The crystalline domain size of MMT/DMSO composites derived from the Scherrer analysis expanded steadily from 2.7 to 10.0 nm with increased DMSO content. The combination of the increased d-spacing and the crystalline domain size upon the addition of DMSO is further evidenced by the increment of the total thickness of the films (Figure S1, Supporting Information). This structured MMT/DMSO film should differ from an immiscible-stacked MMT structure on the matrix and a fully exfoliated uniform MMT distribution on the matrix. Rather, the intercalated DMSO molecules are uniformly ordered on the gallery spaces to form a homogeneously layered MMT structure.

The cross-sectional morphology of MMT and MMT/DMSO composites films was observed by SEM as represented in Figure 3. The images reveal distinct layered structures in the MMT/DMSO composites, which are comparable with the brickand-mortar structure of natural nacre, with the inorganic MMT platelets preferentially stacked horizontally. Starting from the densely packed cross-sectional surface of the pristine MMTs, the MMT/DMSO-5, MMT/DMSO-10, and MMT/DMSO-20 samples have longer distances between the MMT platelets and have a more roughened cross-sectional surface. For the MMT/ DMSO-35 and MMT/DMSO-50 samples, the MMT platelets look like swollen and expanded with excess DMSO. The roughened interlayer surfaces can be attributed to strong interactions between layers which evidently affect the mechanical properties of the composites. Undoubtedly, the ordered DMSO confined by MMT layers plays binding roles in the composites, and excess DMSO deteriorates their binding interactions, which correlates with the XRD structural analysis.

3.2. Thermal Behaviors of MMT/DMSO Composites

To understand the interactions of ordered DMSO confined in MMT structures, the thermal behaviors of the MMT/DMSO composites were investigated by TGA, DTA, and DSC with varying DMSO content as shown in **Figure 4**. The TGA results

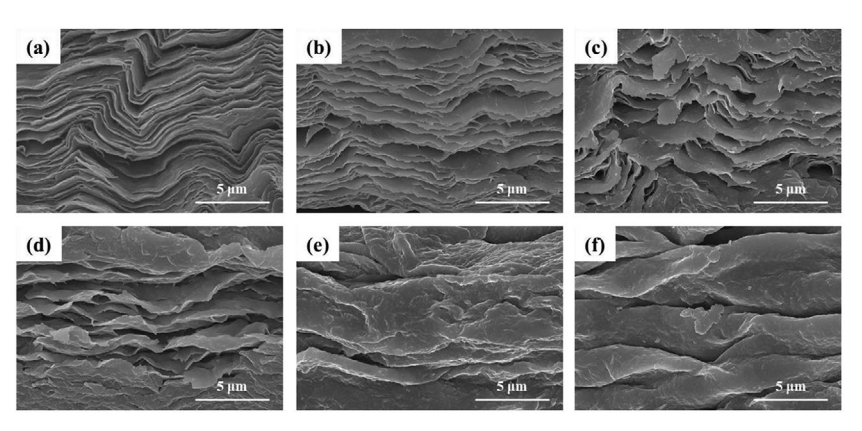


Figure 3. Cross-sectional SEM images of MMT/DMSO composites with varying amounts of DMSO. a) MMT film, b) MMT/DMSO-5, c) MMT/DMSO-10, d) MMT/DMSO-20, e) MMT/DMSO-35, and f) MMT/DMSO-50.

www.advancedsciencenews.com www.advsustainsys.com

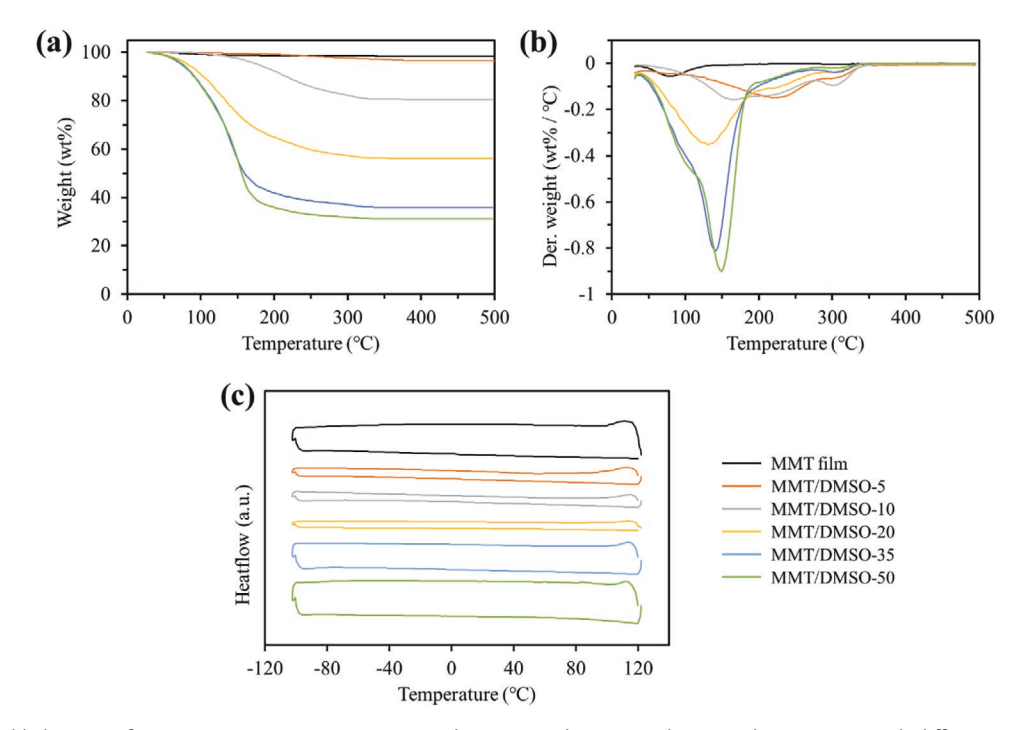


Figure 4. Thermal behaviors of MMT/DMSO composites presented as a) TGA, b) DTA, and c) DSC thermograms with different DMSO contents.

reveal the amount of intercalated DMSO in MMT/DMSO composites as well as their thermal stabilities. Figure 4a shows the weight losses from thermal decomposition of MMT/ DMSO composites as a function of temperature in the range between 30 and 500 °C. At 500 °C, ≈98.2 wt% of residues for neat MMT film is measured, while ≈96.6, ≈80.4, ≈56.1, 35.9, and 31.1 wt% are observed for MMT/DMSO-5, MMT/DMSO-10, MMT/DMSO-20, MMT/DMSO-35, and MMT/DMSO-50, respectively. These results indicate the amount of DMSO intercalated between the MMT layers. Furthermore, thermal destructuring of confined DMSO between MMT layers was measured by DTA, by the onset and peak temperatures. Weight losses of the MMT/DMSO films indicate simple evaporation of DMSO caused by destructuring of the confined DMSO structure. The onset temperature shifts from ≈220 to ≈130 °C with increasing DMSO content from ordered confinement to excess DMSO in the composites (Figure 4b). These lowered onset temperatures likely originated from the partial evaporation of disordered free DMSO. Interestingly, however, the barrier properties of MMT platelets prevent radical decomposition under 100 °C. Rather, MMT layers could form and retain the ordered DMSO in their structures above 130 °C. In DSC measurements, both MMT film and MMT/DMSO composites demonstrated superior thermal stability without any peak in the temperature range of -100 to 120 °C. As can be seen from the TGA results, below 130-150 °C, the temperature at which major decomposition occurs, MMT layers effectively prevent DMSO evaporation without any reaction involving heat transfer. Thus, both the TGA and DSC results demonstrate the sufficiently wide operating temperature range of MMT/DMSO composites, which is important for its use as a solid-state ionic conductor.

The gradually suppressed DSC curves of MMT/DMSO-5, MMT/DMSO-10, and MMT/DMSO-20 suggest the restrained

mobility of confined DMSO in its crystallized state. This efficient binding action by ordered DMSO might be synergistically reinforced by strong hydrogen bonding between the negatively charged MMT clay layers containing -OH groups and DMSO in addition to ionic bonding and van der Waals interactions. The broad vibration of the -OH approximately at 3100–3500 cm⁻¹ confirms the existence of hydrogen bonding between DMSO and MMT platelets (Figure S2, Supporting Information). The bounded mobility of confined DMSO is enhanced with excess DMSO which broadens the interplanar spacing with its relatively high volume originated from several free molecules.

3.3. Mechanical Properties of MMT/DMSO Composites

Next, we investigated the effect of DMSO on the mechanical properties of MMT/DMSO composites by evaluating their strength, modulus, strain to failure, and toughness (Figure 5). In general, MMT hybrid nanocomposites with a high-volume fraction of inorganic component showed high strength, while exhibiting low toughness due to brittleness. As can be seen from Figure 5b, the tensile strength of the MMT/DMSO composites was significantly enhanced with increasing DMSO amount up to 20%. The tensile strength of MMT film and MMT/DMSO-5 were similar which are 23.27 ± 8.87 and 22.63 ± 5.60 MPa, respectively. It increased up to 55.32 ± 4.79 MPa for MMT/DMSO-20 and then decreased to 2.73 \pm 0.09 MPa with the excess of DMSO in the composites. Similarly, except the brittle MMT film, the trend of Young's modulus change of MMT/DMSO composites correlated with the sample's strength (Figure 5c). The maximum tensile strength and Young's modulus were observed for MMT/DMSO-20, which seems to be related to both the hydrogen bonding

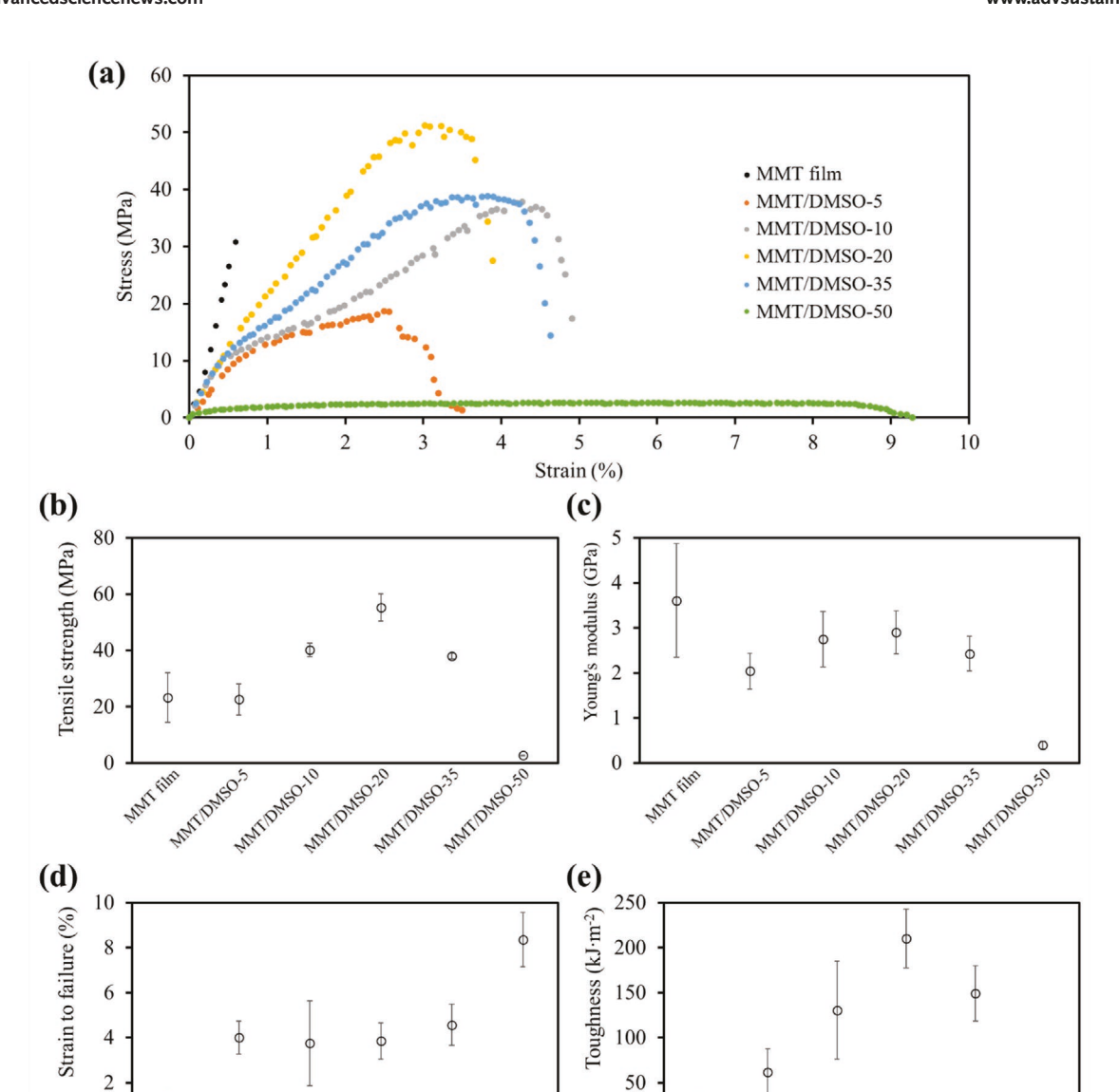


Figure 5. Mechanical performances of MMT/DMSO composites. a) Stress-strain curve, b) tensile strength, c) Young's modulus, d) strain to failure, and e) toughness of MMT/DMSO composites as a function of DMSO content.

MATTER SO.5

MMI film

0

WWW.DW.

WHILD WE O'TO

MMIDNEO 35

NATIONS OF SO

between MMT platelets and that between MMT platelets and DMSO. This is consistent with the short interplanar distances of MMT/DMSO-20 revealed from XRD analysis.

MATIONSO'S

MATTON SO. 10

WWW. DW. O. TO

MMIDNSO.35

0

As shown in Figure 5d, extensional properties were improved as evident from the increased strain-to-failure to 8.36 \pm 1.22% upon the addition of DMSO up to 50%, indicating a significant increase of film flexibility, to more than seven times higher than pure MMT film (1.17 \pm 0.23%). Basically, the molecular proximity of the nanoconfined crystal structure of MMT/DMSO composites seems to affect the strain-to-failure by providing effective stress-transfer sites. The remarkable increase in the strain-to-failure value of MMT/DMSO-50 is further attributed to the excess DMSO molecules, which can move around the MMT galleries more freely, unlike many other polymers. Furthermore, the bonds between DMSO molecules tend to rearrange easily when they were disconnected, thereby contributing to the enhanced strain-to-failure values as compared with high molecular weight entangled polymer chains. The average toughness first increased from 19.76 \pm 16.31 to 210.21 \pm 32.55 kJ m⁻², and then decreased to $21.71 \pm 2.53 \text{ kJ} \text{ m}^{-2}$ with DMSO content as plotted in Figure 5e. Evidently, the DMSO content for optimal mechanical properties was again found at MMT/DMSO-20, when MMT platelets were orderly packed together with extremely thin DMSO layers to form MMT/DMSO complex, leading to high mechanical properties at the interface. DMSO possesses comparable surface tension energy (≈44 mN m⁻¹ in air), which

MARTIDASO 50

ADVANCED SUST AINABLE SYSTEMS

facilitates strong interfacial interactions and uniform intercalation into MMT. However, mechanical properties deteriorated when the amount of input DMSO was larger than 20% because excess DMSO failed to form a complex with the MMT as well as significantly low mechanical properties of bulk DMSO liquid.

3.4. Electrochemical Performances of MMT/DMSO Composites

We have also investigated the electrochemical impedance of DMSO intercalated MMT nanocomposites at room temperature, 20 °C. From the EIS spectra (Figure 6a), a dramatic decrement of impedance was observed with increasing DMSO in MMT/DMSO composites across the whole frequency range. As shown in the Bode plot with phase angles, the MMT-only film behaves in rather a capacitive way over the whole frequency range as an insulator. On the other hand, the MMT/DMSO composites tend to behave in a more resistive manner than a capacitive way at the high-frequency range with increasing DMSO content. This change might be triggered because confined DMSO in the composites provides the local dielectric that induces charge polarization subsequently generating effective charge carriers through less insulating sites. This ionic transport is unique because the overall impedance spectra of MMT/ DMSO composites are much lower than those of MMT/lactic acid composites with a surface energy of ≈ 70.7 mN m⁻¹ (Figure S3, Supporting Information). Moreover, the ionic conductivity of MMT/DMSO composites was calculated by considering the film thickness, the electrode area, and the impedance of the real axis at the inflection point (Figure 6b).

$$\sigma = \frac{1}{R} \times \frac{L}{S} \tag{4}$$

where R is the resistance calculated from the real axis, L is the thickness of the film, and S is the contact area between the film and electrodes. The internal resistance composed of the electrode–electrolyte interfacial resistance and the electrolyte-bulk resistance can be calculated from the value of Z' exists. [80] Here, the ionic conductivity of MMT/DMSO increased with the amount of DMSO in the film up to 2.06×10^{-4} S cm $^{-1}$ at MMT/DMSO-50. The positive relationship between the content of DMSO and the conductivity is consistent with the result of XRD analysis that reveals the crystalline domain size of MMT/DMSO composites.

From the EIS, the charge transport mechanism for MMT/ DMSO composites can be divided into two processes: ionic hopping at confined MMT/DMSO lattice structure and ionic migration along the excess DMSO^[81-83] (Figure S5, Supporting Information). The ionic conductivity of the confined structure is dominantly attributed to ionic hopping processes. Since MMT has exchangeable sites for holding cation, the Na⁺ ions can hop into neighboring sites along the MMT lattices by applying local charge potential.[81,84] Furthermore, confined DMSO forms localized charge potential to drive Na⁺ hopping by dielectric barriers among MMT lattices. Subsequently, molecularly confined DMSO dielectrics along the MMT lattices which accommodate a significant amount of the Na+ ions, greatly affect the charge transfer efficiency. On the other hand, as increasing DMSO content, the amount of Na⁺ ions in the DMSO phase grows to long-range ionic migration while the ionic solubility in DMSO is quite limited. In the DMSO phase, Na⁺ ions migrate along the favorable pathways provided by excess DMSO. These synergistic mechanisms of ionic transports contribute to increasing overall ionic conductivities as well as to decrease the impedance. Note that the overall charge conductivities at pure DMSO were extremely poor. Therefore, the addition of DMSO to the

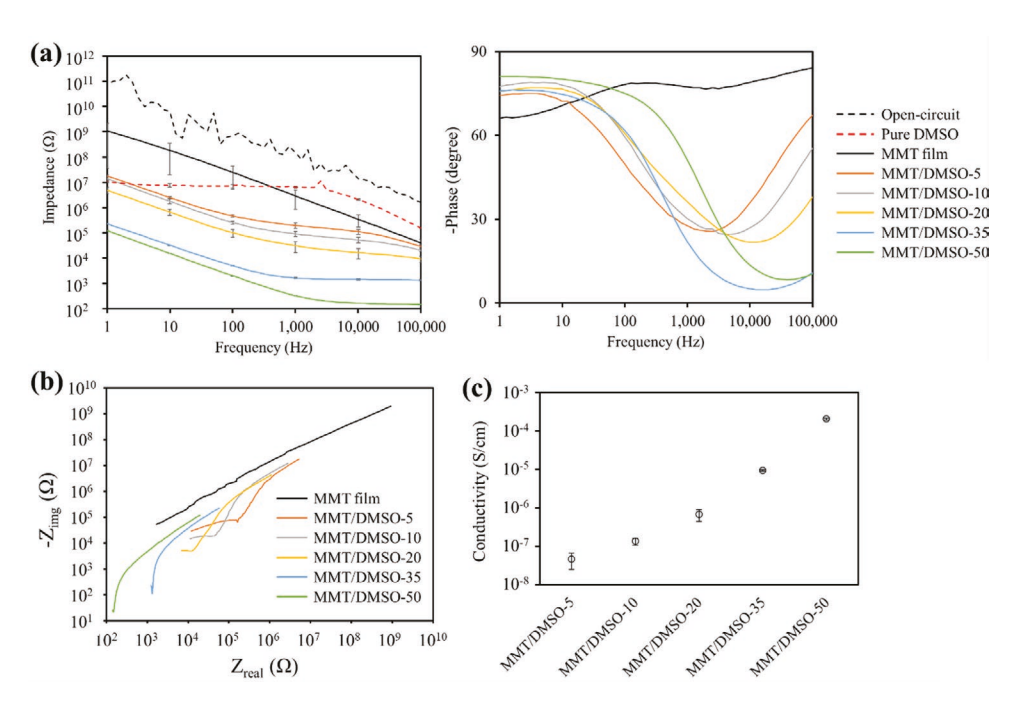


Figure 6. Electrochemical performances of MMT/DMSO composites. a) Bode plot and b) Nyquist plot with a logarithmic scale, and c) conductivity of MMT/DMSO composites as a function of DMSO content.

ADVANCED SUST AINABLE SYSTEMS

MMT/DMSO composites causes both ionic migration and ionic hopping mechanisms, resulting in reducing the impedance spectra across the entire measured frequency range.

The theoretical number of Na⁺ ions in MMT lattice is 0.33 per unit chemical formula, which is a good number of mobile ions to be an electrolyte. To be sure, we have measured the Na⁺ concentration in the solution with inductively coupled plasma (ICP) analysis. The average concentration of Na⁺ ions in MMT lattice was measured to be 42.72 \pm 0.96 μg mm⁻³ MMT.

To prove that major charge-carrying ions are Na⁺ in the MMT/DMSO composite, we have further tested EIS and calculated bulk conductivity after adding excess Na+ ions in the MMT/DMSO (Figure S6, Supporting Information). To add excess Na+ ions to the system, NaCl were dissolved in the MMT solution during the composite preparation. Even after making an MMT/DMSO composite with excess NaCl, there was no remarkable change of the conductivity, rather slight decreases of ionic conductivities were shown. This example proves that our MMT/DMSO films are already saturated with Na⁺ on MMT lattice and very low solubility of Na⁺ on DMSO because excess Na⁺ could not contribute to increasing the conductivities. The reference value of Na+ solubility in DMSO at 20 °C is just 1.57 µg mm⁻³ DMSO, which is at least 20 times lower solubility than in MMT lattice. This solubility difference indicates that majorities of charge-carrying Na+ ions exist in MMT lattice and, thus Na+ ions transfer among the MMT lattices. The role of confined DMSO in the gallery space of MMT is to bring localized dielectric potential to drive mobile Na⁺ ion hopping among the MMT lattices. Because the solubility of charged ions on DMSO is very low, there is practically no physical space for accommodating H+ ions without replacing Na+ on the MMT lattice. This vacancy of ions in DMSO solution is evidenced by the extremely high impedance spectrum of pure DMSO as shown in Figure 6a.

Another proof that the charge conductivity contribution from H⁺ is very limited was suggested by EIS results of MMT/lactic acid in Figure S3 (Supporting Information). Even though lactic acid is a good source of H⁺ ions, their impedances were much higher than the MMT/DMSO. While hygroscopic behavior of the MMT/DMSO composites could bring potential H⁺ ions in the ionic conductivities, we have completely dried the composites in a drying oven before measuring the EIS. Thus, the contribution to ionic conductivity by H⁺ is extremely limited even if not being completely excluded.

As shown in Figure 5, MMT/DMSO composites which do not contain excess DMSO are relatively mechanically stiff compared to those containing excess DMSO. This may have affected the poor contact between the composite and the electrodes, which directly induces the high interfacial impedance. For the more accurate fitting, further experiments are necessary after sufficiently improving their interfacial impedance. Thus, we have here only considered MMT/DMSO-35 and MMT/DMSO-50. The equivalent circuits models were composed of contact resistance (R_c), conduction resistances (R_1 , R_2), and inner capacitances (C_1 , C_2).

The detailed circuit parameters and goodness of fit are shown in Table S1 (Supporting Information). The contact resistances of both MMT/DMSO-35 and MMT/DMSO-50 are lower than 1.5 k Ω which are negligible compared with the other resistance parameters. All resistance and capacitance parameters of MMT/DMSO-50 were calculated to be lower and higher than those of MMT/DMSO-35, respectively. The most significant difference between MMT/DMSO-20, MMT/DMSO-35, and MMT/DMSO-50 was in the amount of excess DMSO. Similar to impedance and conductivity changes, in this simulation and fitting, it was demonstrated that the excess DMSO plays major role in charge conduction.

3.5. Biodegradability Test

The biodegradabilities of MMT film and MMT/DMSO composites were tested by feeding them to 40 superworms for 4 h at room temperature. The weight drop of the films was measured 4 h after putting both superworms and films together in the cage (Figure 7a). The superworms like to eat all of the films, but prefer the softer films. One superworm eats about 0.59 mg of pure MMT film an hour on average, while they ingest 0.49 mg of MMT/DMSO-20 and 0.78 mg of MMT/DMSO-50 which were the most rigid and softest one among the MMT/DMSO composites, respectively. Figure 7b shows the digital image of superworms in the cage and the films after feeding. The worms prey on the films by chewing from the edge and egest them into the biomass.

3.6. Flame-Retardant Ability and Flexibility of MMT/DMSO Composites

The foldability, flexibility, and flame-retardant properties of MMT/DMSO composites were studied in detail with the MMT/DMSO-20 sample which showed superior mechanical properties over the other MMT/DMSO composites. The MMT/DMSO-20 was exposed to the flames of a gas torch and began to burn, but immediately self-extinguished upon the removal of the flame as shown in **Figure 8**a. Although DMSO itself is a highly inflammable organic solvent, we noted that MMT/DMSO-20 films which contain around 40 wt% of DMSO

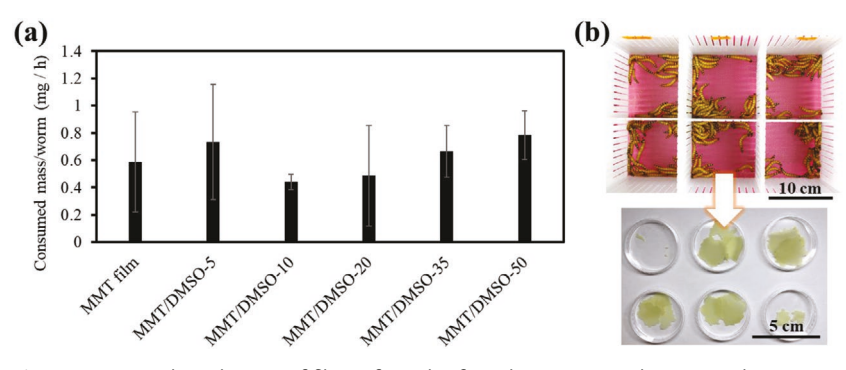
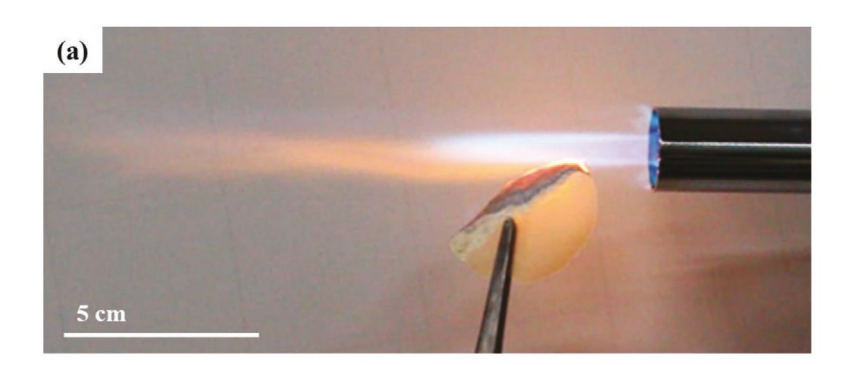
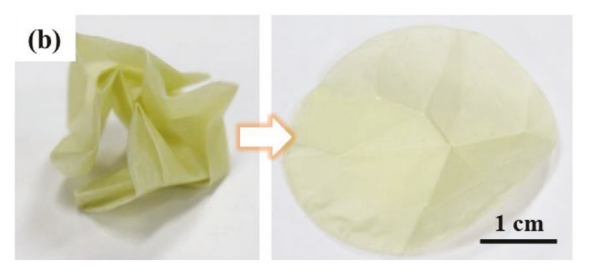


Figure 7. a) Weight reduction of films after 4 h of residence time in the cage with 40 superworms. b) Digital image of superworms and cut films immediately after placing films into the cage (left) and after 4 h (right).

www.advsustainsys.com







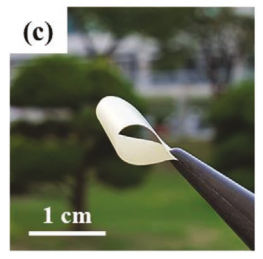


Figure 8. Photographs of freestanding MMT/DMSO composites showing a) fire-retardant property, b) foldability, and c) flexibility.

confirmed by TGA analysis showed self-extinguishing behavior. This flame-retardant behavior can be explained by the hierarchical structure (macroscopic roughened structure together with nanoscopic aligned layered structure) of the MMT/DMSO composites, which acts as a heat barrier to interfere with advancing and spreading of flames during the burning process. Furthermore, MMT/DMSO composites were foldable and flexible, as represented in Figure 8b,c. The photographs demonstrate that MMT/DMSO composites were able to keep their form even when they were completely crumpled. Notably, our nacre-like MMT/DMSO composites show pronounced flexibility compared with natural nacre.

The obtained MMT/DMSO composites were optically translucent as presented in Figure S8 (Supporting Information), implying flat and uniform alignment of the MMT-DMSO platelets. Altogether, the data show that MMT/DMSO composites are benign fire-retardant materials. A further advantage of these biomimetic MMT/DMSO composites over conventional flame-retardants is their facile and environmentally friendly preparation processes.

4. Conclusion

Nacre-mimetic MMT/DMSO composites with a brick-and-mortar structure were successfully fabricated through a vacuum-assisted filtration process. Reinforcement of MMT/DMSO composites was affected by interfacial interactions, such as hydrogen bonding, ionic bonding, and van der Waals interactions between the constituents. The MMT/DMSO composites were compactly stacked and regularly aligned along the in-plane direction. XRD analysis showed the intercalation of DMSO into layered MMT platelets as confirmed by a change of the interlayer *d*-spacing and crystalline domain size. This nanoconfinement effect is presented with

the maximum peak intensity of MMT/ DMSO-20 in the XRD pattern. The molecular structural ordering of the layered nanoarchitecture was associated with the mechanical enhancement of the composites including tensile strength, Young's modulus, strain-to-failure, and toughness. In addition, the ionic conductivity of the composite revealed excellent electrochemical properties at room temperature. These nanocomposite films were demonstrated to be thermally stable over a temperature range of -100 to 120 °C by DSC analysis and were able to demonstrate on-demand degradation when fed to superworms. The MMT/DMSO composites were also translucent, flexible, and flame-retardant. This work based on nanoconfinement of DMSO molecules highlights a simple and efficient approach for further development of bioinspired structural materials with multifunctional performance.

Supporting Information

Supporting Information is available from the Wiley Online Library or from the author.

Acknowledgements

This work was supported by the National Research Foundation of Korea (NRF) grant funded by the Korea government (MSIT) (Basic Research Program: NRF-2017R1A2B4012736), by a grant from the AFRL AFOSR Joint Program NRF-2018K1A3A1A32055149, and by a planning grant from NRF-2019M3D1A2103919.

Conflict of Interest

The authors declare no conflict of interest.

Keywords

biodegradable, composites, eco-friendly materials, ionic conductivity, montmorillonite, nacre-mimetic, solid-state electrolytes

Received: November 22, 2019 Revised: January 26, 2020 Published online:

^[1] M. Keller, A. Varzi, S. Passerini, J. Power Sources 2018, 392, 206.

^[2] S. P. Ong, V. L. Chevrier, G. Hautier, A. Jain, C. Moore, S. Kim, X. Ma, G. Ceder, Energy Environ. Sci. 2011, 4, 3680.

^[3] N. Yabuuchi, K. Kubota, M. Dahbi, S. Komaba, Chem. Rev. 2014, 114, 11636.

^[4] H. Wang, C. Zhu, D. Chao, Q. Yan, H. J. Fan, Adv. Mater. 2017, 29, 1702093

www.advsustainsvs.com

- [5] V. Palomares, P. Serras, I. Villaluenga, K. B. Hueso, J. Carretero-González, T. Rojo, Energy Environ. Sci. 2012, 5, 5884.
- [6] I. Hasa, D. Buchholz, S. Passerini, B. Scrosati, J. Hassoun, Adv. Energy Mater. 2014, 4, 1400083.
- [7] P. Barpanda, G. Oyama, S. I. Nishimura, S. C. Chung, A. Yamada, Nat. Commun. 2014, 5, 4358.
- [8] S. Komaba, W. Murata, T. Ishikawa, N. Yabuuchi, T. Ozeki, T. Nakayama, A. Ogata, K. Gotoh, K. Fujiwara, Adv. Funct. Mater. 2011, 27, 3859.
- [9] B. L. Ellis, L. F. Nazar, Curr. Opin. Solid State Mater. Sci. 2012, 16, 168
- [10] E. Lee, J. Lu, Y. Ren, X. Luo, X. Zhang, J. Wen, D. Miller, A. DeWahl, S. Hackney, B. Key, D. Kim, M. D. Slater, C. S. Johnson, Adv. Energy Mater. 2014, 4, 1400458.
- [11] H. Wang, Y. Xiao, C. Sun, C. Lai, X. Ai, RSC Adv. 2015, 5, 106519.
- [12] H. Li, L. Peng, Y. Zhu, D. Chen, X. Zhang, G. Yu, Energy Environ. Sci. 2016, 9, 3399.
- [13] J. Z. Guo, P. F. Wang, X. L. Wu, X. H. Zhang, Q. Yan, H. Chen, J. P. Zhang, Y. G. Guo, Adv. Mater. 2017, 29, 1701968.
- [14] S. Li, Y. Dong, L. Xu, X. Xu, L. He, L. Mai, Adv. Mater. 2014, 26, 3545.
- [15] C. Zhu, P. Kopold, P. A. Van Aken, J. Maier, Y. Yu, Adv. Mater. 2016, 28, 2409.
- [16] F. Wan, J. Z. Guo, X. H. Zhang, J. P. Zhang, H. Z. Sun, Q. Yan, D. X. Han, L. Niu, X. L. Wu, ACS Appl. Mater. Interfaces 2016, 8, 7790.
- [17] H. Gao, W. Zhou, K. Park, J. B. Goodenough, Adv. Energy Mater. 2016, 6, 1600467.
- [18] J. Ming, H. Ming, W. Yang, W. J. Kwak, J. B. Park, J. Zheng, Y. K. Sun, RSC Adv. 2015, 5, 8793.
- [19] J. B. Goodenough, H.-P. Hong, J. A. Kafalas, Mater. Res. Bull. 1976, 11, 203.
- [20] D. Santhanagopalan, D. Qian, T. McGilvray, Z. Wang, F. Wang, F. Camino, J. Graetz, N. Dudney, Y. S. Meng, J. Phys. Chem. Lett. 2014. 5, 298.
- [21] H. D. Yoo, I. Shterenberg, Y. Gofer, G. Gershinsky, N. Pour, D. Aurbach, Energy Environ. Sci. 2013, 6, 2265.
- [22] R. Sudo, Y. Nakata, K. Ishiguro, M. Matsui, A. Hirano, Y. Takeda, O. Yamamoto, N. Imanishi, Solid State Ionics 2014, 262, 151.
- [23] Y. Ren, Y. Shen, Y. Lin, C. W. Nan, Electrochem. Commun. 2015, 57,
- [24] D. Lin, Y. Liu, Y. Cui, Nat. Nanotechnol. 2017, 12, 194.
- [25] I. Villaluenga, K. H. Wujcik, W. Tong, D. Devaux, D. H. C. Wong, J. M. DeSimone, N. P. Balsara, Proc. Natl. Acad. Sci. USA 2016, 113, 52.
- [26] H. Zhai, P. Xu, M. Ning, Q. Cheng, J. Mandal, Y. Yang, Nano Lett. 2017, 17, 3182.
- [27] A. Arya, A. L. Sharma, Ionics 2017, 23, 497.
- [28] F. Sagane, T. Abe, Y. Iriyama, Z. Ogumi, J. Power Sources 2005, 146, 749.
- [29] A. Manthiram, X. Yu, S. Wang, Nat. Rev. Mater. 2017, 2, 16103.
- [30] E. Quartarone, P. Mustarelli, Chem. Soc. Rev. 2011, 40, 2525.
- [31] Y.-S. Hu, Nat. Energy 2016, 1, 16042.
- [32] J. W. Fergus, J. Power Sources 2010, 195, 4554.
- [33] W. Xia, B. Xu, H. Duan, Y. Guo, H. Kang, H. Li, H. Liu, ACS Appl. Mater. Interfaces 2016, 8, 5335.
- [34] T. Matsuyama, A. Sakuda, A. Hayashi, Y. Togawa, S. Mori, M. Tatsumisago, J. Solid State Electrochem. 2013, 17, 2679.
- [35] C. Monroe, J. Newman, J. Electrochem. Soc. 2005, 152, A396.
- [36] E. Munch, M. E. Launey, D. H. Alsem, E. Saiz, A. P. Tomsia, R. O. Ritchie, *Science* 2008, 322, 1516.
- [37] H. D. Espinosa, J. E. Rim, F. Barthelat, M. J. Buehler, *Prog. Mater. Sci.* 2009, 54, 1059.
- [38] M. I. López, M. A. Meyers, Mater. Sci. Eng., C 2016, 58, 7.
- [39] J. Wang, Q. Cheng, L. Lin, L. Jiang, ACS Nano 2014, 8, 2739.

- [40] T. U. Patro, H. D. Wagner, Nanotechnology 2011, 22, 455706.
- [41] P. Podsiadlo, S. Paternel, J. M. Rouillard, Z. Zhang, J. Lee, J. W. Lee, E. Gulari, N. A. Kotov, *Langmuir* 2005, 21, 11915.
- [42] P. Podsiadlo, A. K. Kaushik, E. M. Arruda, A. M. Waas, B. S. Shim, J. Xu, H. Nandivada, B. G. Pumplin, J. Lahann, A. Ramamoorthy, N. A. Kotov, *Science* 2007, 318, 80.
- [43] S. Deville, E. Saiz, R. K. Nalla, A. P. Tomsia, Science 2006, 311, 515.
- [44] O. Oner Ekiz, A. F. Dericioglu, H. Kakisawa, Mater. Sci. Eng. C 2009, 29, 2050.
- [45] S. Huang, Z. Yang, H. Zhu, L. Ren, W. W. Tjiu, T. Liu, Macromol. Res. 2012, 20, 568.
- [46] S. Nayar, A. K. Pramanick, A. Guha, B. K. Mahato, M. Gunjan, A. Sinha, Bull. Mater. Sci. 2008, 31, 429.
- [47] Y. Q. Li, T. Yu, T. Y. Yang, L. X. Zheng, K. Liao, Adv. Mater. 2012, 24, 3426.
- [48] S. Wan, J. Peng, Y. Li, H. Hu, L. Jiang, Q. Cheng, ACS Nano 2015, 9, 9830.
- [49] M. Mirkhalaf, F. Barthelat, J. Mech. Behav. Biomed. Mater. 2016, 56, 23
- [50] K. M. Nam, Y. J. Lee, W. T. Kwon, S. R. Kim, D. G. Shin, H. M. Lim, H. Kim, Y. Kim, J. Korean Ceram. Soc. 2014, 51, 7.
- [51] C. A. Wang, Y. Huang, Q. Zan, L. Zou, S. Cai, J. Am. Ceram. Soc. 2002, 85, 2457.
- [52] X. Zeng, L. Ye, S. Yu, H. Li, R. Sun, J. Xu, C. P. Wong, Nanoscale 2015. 7, 6774.
- [53] Y. Shu, P. Yin, B. Liang, H. Wang, L. Guo, ACS Appl. Mater. Interfaces 2014 6 15154
- [54] F. De Luca, R. Menzel, J. J. Blaker, J. Birkbeck, A. Bismarck, M. S. P. Shaffer, ACS Appl. Mater. Interfaces 2015, 7, 26783.
- [55] Y. Shu, P. Yin, B. Liang, H. Wang, L. Guo, *Ind. Eng. Chem. Res.* 2015, 54, 8940.
- [56] Q. Cheng, M. Wu, M. Li, L. Jiang, Z. Tang, Angew. Chem., Int. Ed. 2013, 52, 3750.
- [57] Q. Cheng, J. Duan, Q. Zhang, L. Jiang, ACS Nano 2015, 9, 2231.
- [58] K. M. Nam, Y. J. Lee, W. T. Kwon, S. R. Kim, H. M. Lim, H. Kim, Y. Kim, J. Korean Ceram. Soc. 2012, 49, 438.
- [59] A. Jayaraman, G. Subramanyam, S. Sindhu, P. K. Ajikumar, S. Valiyaveettil, Cryst. Growth Des. 2007, 7, 142.
- [60] Z. Tang, N. A. Kotov, S. Magonov, B. Ozturk, Nat. Mater. 2003, 2, 413.
- [61] L. P. Xu, J. Peng, Y. Liu, Y. Wen, X. Zhang, L. Jiang, S. Wang, ACS Nano 2013, 7, 5077.
- [62] Q. Y. Soundararajah, B. S. B. Karunaratne, R. M. G. Rajapakse, J. Compos. Mater. 2010, 44, 303.
- [63] D. S. Aldana, E. D. Villa, M. D. D. Hernández, G. G. Sánchez, Q. R. Cruz, S. F. Gallardo, H. P. Castillo, L. B. Casarrubias, *Polymers* 2014, 6, 2386.
- [64] J. Zhu, A. B. Morgan, F. J. Lamelas, C. A. Wilkie, Chem. Mater. 2001, 13, 3774.
- [65] P. Kiliaris, C. D. Papaspyrides, Prog. Polym. Sci. 2010, 35, 902.
- [66] P. Das, J. M. Malho, K. Rahimi, F. H. Schacher, B. Wang, D. E. Demco, A. Walther, *Nat. Commun.* 2015, 6, 5967.
- [67] J. D. Dana, E. S. Dana, W. E. Ford, Dana's System of Mineralogy, Wiley, New York 1909.
- [68] H. Deer, R. A. Howie, Ortho- and Ring Silicates, Longman, London 1962.
- [69] J. W. Earley, B. B. Osthaus, I. H. Milne, Am. Mineral. 1953, 38, 707.
- [70] E. P. Giannelis, Adv. Mater. 1996, 8, 29.
- [71] Y. Xu, X. Ren, M. A. Hanna, J. Appl. Polym. Sci. 2006, 99, 1684.
- [72] S. C. Tjong, Mater. Sci. Eng., R 2006, 53, 73.
- [73] F. Carosio, J. Kochumalayil, F. Cuttica, G. Camino, L. Berglund, ACS Appl. Mater. Interfaces 2015, 7, 5847.
- [74] A. Yasmin, J. L. Abot, I. M. Daniel, Scr. Mater. 2003, 49, 81.
- [75] X. Jia, Y. Li, B. Zhang, Q. Cheng, S. Zhang, Mater. Res. Bull. 2008, 43, 611.



www.advancedsciencenews.com www.advsustainsys.com

- [76] R. Merindol, S. Diabang, O. Felix, T. Roland, C. Gauthier, G. Decher, ACS Nano 2015, 9, 1127.
- [77] H. H. Szmant, Ann. N. Y. Acad. Sci. 1975, 243, 20.
- [78] D. Burgentzlé, J. Duchet, J. F. Gérard, A. Jupin, B. Fillon, J. Colloid Interface Sci. 2004, 278, 26.
- [79] J. I. Langford, A. J. C. Wilson, J. Appl. Crystallogr. 1978, 11, 102.
- [80] B. A. Mei, O. Munteshari, J. Lau, B. Dunn, L. Pilon, J. Phys. Chem. C 2018, 122, 194.
- [81] D. P. Almond, C. C. Hunter, A. R. West, J. Mater. Sci. 1984, 19, 3236.
- [82] A. Lasia, Electrochemical Impedance Spectroscopy and Its Applications, Springer-Verlag, New York 2014.
- [83] V. S. Bagotsky, Fundamentals of Electrochemistry, 2nd ed, Wiley, New York 2005.
- [84] T. M. Lai, M. M. Mortland, Soil Sci. Soc. Am. J. 1961, 25, 353.